Understanding the oxidation resistance of zirconium alloy at 1000 ℃ based on the formation of a Zr-Sn intermetallic phase and co-precipitation of Sn and Nb

Zhexin Cui[a,b], Junkai Liu[c], Guangdong Liu[d], Guogao Tang[e], Xiaochun Liu[e], Ruizhi Meng[a], Sergio Lozano-Perez[b], Di Yun[a,f,*], Huiqiu Deng[d,*]

[a] *School of Nuclear Science and Technology, Xi'an Jiaotong University, Xi'an 710049, China*

[b] *Department of Materials, University of Oxford, Parks Road, Oxford OX1 3PH, UK*

[c] *School of Advanced Materials and Nanotechnology, Xidian University, Xi'an 710126, China*

[d] *School of Physics and Electronics, Hunan University, Changsha 410082, China*

[e] *Institute of Metals, College of Materials Science and Engineering, Changsha University of Science and technology, Changsha 410082, China*

[f] *Key Laboratory of Thermo-Fluid Science and Engineering of MOE, School of Energy and Power Engineering, Xi'an Jiaotong University, Xi'an 710049, PR China*

* *Corresponding author. E-mail address: diyun1979@xjtu.edu.cn (Di Yun) and hqdeng@hnu.edu.cn (Huiqiu Deng);*

Abstract

The oxidation behavior of zirconium alloy in high-temperature steam plays a dominant role in the operation of nuclear reactors under accident conditions. The present work investigated the effect of Sn on the oxidation behavior of zirconium alloys in high-temperature steam at 1000℃. The results of scanning electron microscopy (SEM), metallographic microscopy and synchrotron X-ray diffraction (S-XRD) analyses show that there are three layers in the oxidized sample, including prior β-Zr, α-Zr(O) and ZrO_2. High resolution analyses conducted in these layers by transmission electron microscopy (TEM) show that Sn atoms segregate around the oxide-metal (O-M interface and Zr-Sn intermetallic precipitates only present in the oxide film. Clear atomic arrangements of Zr_5Sn_3 were obtained by TEM, resulting in accurate identification of the Zr-Sn intermetallic phase. Also, TEM energy dispersive spectroscopy (EDS) maps show that Zr-Sn particles invariably accompany the segregation or precipitation of Nb. However, no clear precipitation sequence was observed, which suggests that a co-precipitation mechanism of Sn and Nb is in operation. As oxidation proceeds, nanovoids next to the Zr-Sn intermetallic particles were observed accompanied by local areas deficient in oxygen, identified as ZrO. Combining the interdiffusion trend obtained by Density functional theory (DFT) and

ab initio molecular dynamics (AIMD) simulations, a mechanism for the transformation from the Zr-Sn intermetallic precipitates to nanovoids was proposed. This proposed mechanism may shed new light into the role of Sn in the oxidation resistance of zirconium alloy under LOCA conditions.

Key words: Zirconium alloy, high-temperature oxidation, effect of tin, nanovoids

1. Introduction

Zirconium alloys are used for light-water reactor cladding tubes due to their excellent properties, especially its low absorption cross section for thermal neutrons. As cladding tubes, the structural integrity needs to be guaranteed, since fuel pellets must be well contained to prevent possible reaction with water and the leakage of radioactive products. However, oxidation interactions between cladding and coolant triggered by high temperature would decrease the effective thickness of the cladding tubes and degrade its protective function [1]. This process is accelerated dramatically under high-temperature oxidation conditions [2,3] during the loss-of-coolant accidents (LOCA) in pressurized water reactors (PWRs). At temperatures lower than 1200 ˚C (the transformation temperature from the tetragonal to monoclinic phase of ZrO_2), there is a general consensus that decreasing the Sn content would improve the oxidation resistance of zirconium alloys [2–4]. Also, the addition of Sn into Zr-Nb alloys would degrade the oxidation resistance, under both normal service or LOCA conditions [5–7]. However, the exact underlying mechanism leading to the different oxidation performance caused by Sn is still not well understood, especially for the LOCA condition in PWRs.

The impact of Sn on oxidation behavior has been widely studied under normal operating conditions around 360 ˚C. Initially, Sn was added to zirconium alloys to deal with the effects of nitrogen impurities and to enhance the mechanical properties [8–11], which led to the development of Zr-Sn alloys. However, later experiments [2,10] suggested that a further increase in Sn content was detrimental to the oxidation

resistance, leading to the development and application of a series of zirconium alloy with low Sn content (around 1 wt%). At this level, Sn tends to completely dissolve into the Zr lattice [8,12] and its role in corrosion is less clear than elements such as Nb, Fe, and Cr that are incorporated into second phase particles (SPPs) [13–16]. Recently, the relationship between Sn and the stabilization of the tetragonal form of the oxide, t-ZrO_2, has been investigated. Normally, t-ZrO_2 is considered as the protective barrier to oxidation [17–19] stabilized by compressive stress [20–24], grain size [20,21], chemical dopants [25,26] and vacancies [27–29]. However, its transformation from the tetragonal phase to the monoclinic phase (m-ZrO_2) is regarded as a possible mechanism for breakaway oxidation [23,30,31]. It has been observed that a reduction in Sn content caused an increase in the fraction of t-ZrO_2 [2]. As a heterovalent dopant in the oxide, Sn ions can introduce charged vacancies, one of the stabilizers of t-ZrO_2, to maintain electric neutrality. [25,27,32]. Moreover, the density functional theory (DFT) simulations by Bell [33] emphasized that the Sn^{2+} ions tended to bind with vacancies and transform to Sn^{4+} when the oxygen partial pressure exceeds a critical value. Nevertheless, all these researches are based on the service condition, further investigation are required for the accident conditions.

At higher temperatures, increasing Sn content also contributes to faster oxidation kinetics [34,35]. However, in contrast to normal service conditions, Raman spectra obtained in the range of 800-1000 ˚C showed that t-ZrO_2 became increasingly difficult to observe with the increase of temperature[36]. Thus, at higher temperature, the t-m transformation of ZrO_2 may not play a dominant role in oxidation resistance, and so this mechanism cannot be responsible for the effect of Sn on the oxidation behavior. The observation of Sn segregation in zirconia during high-temperature steam oxidation experiments [37–41] and annealing experiments [42] might provide a new standpoint for us to understand the role of Sn in the high-temperature oxidation of zirconium alloys. Pawel et al. [40], Dobson et al. [41] and Grosse et al. [38] observed remarked segregations of Sn parallel to the oxide-metal (O-M) interface in the oxide formed on cladding tubes when the temperature exceeded 1300 ˚C. Pawel et

al. [40] suggested that the oxide film had a tendency to spall off along this Sn-rich line. Meanwhile, Lee et al. [37] found that Zr_5Sn_3 and $ZrSn_2$ precipitates formed at oxide grain boundaries at 1200 ˚C. They argued that these particles along grain boundaries impeded the diffusion of oxygen and thus improved the oxidation resistance. However, insufficient experimental evidence was provided to support their hypothesis on the effect of Sn on the oxidation behavior of zirconium alloys. At lower temperatures, there are also several groups reporting the existence of Sn segregation. Dong et al. [43] reported the segregation of Sn in oxide at 360 ˚C through ATP experiments. Due to lack of transmission electron microscopy (TEM) results, their conclusion that Sn segregations was located at grain boundaries was based on the similarity of the spacing between Sn segregation and the width of oxide grains in the same sample. Furthermore, DFT simulations conducted by Yuan et al. [44] indicated that Sn atoms have a 100% likelihood to segregate to ZrO_2 grain boundaries at 633 and 673 K. Because of the rare observation of Sn segregation or Zr-Sn intermetallic particles at low temperatures, their existence in the oxide under normal operation conditions is currently unclear. In addition, the structural complexity of Zr-Sn binary phases [45] and the small size of segregation at lower temperatures render phase identification rather challenging. From this summary, it is clear that further investigation in the behavior of Sn atoms is needed over the full range of possible in-reactor temperatures.

In this work, ZIRLO, a commercial Zr-Sn-Nb alloy, was used to investigate the influence of Zr-Sn intermetallic precipitation on the oxidation behavior of zirconium alloys at 1000 ˚C in high-temperature steam. To record the evolution of Zr-Sn intermetallic phases and nanovoids in oxide film at different oxidation stages, six specimens were prepared and characterized by metallographic microscope, scanning electron microscope (SEM), TEM, spherical aberration corrected transmission electron microscope (ACTEM) and synchrotron X-Ray diffraction (S-XRD). DFT and ab initio molecular dynamics (AIMD) simulations were also conducted to obtain a deeper insight into the dynamic evolution of Zr-Sn intermetallic phases during

oxidation. Integrating all the results, a new mechanism is proposed to explain the impact of Sn on oxidation resistance at high temperatures based on the evolution of Zr-Sn precipitation and the formation of nanovoids.

2. Method

2.1 High-temperature steam oxidation test

The cladding tube used in the present research is commercial ZIRLO (Zr-1Nb-1Sn-0.1Fe) with 9.5 mm outer diameter and 0.5 mm wall thickness. The tubes were cut into shorter ones of 15 mm in length so that they could be accommodated by the instruments. Before the oxidation experiments, acid pickling with a mixed acid solution (volume ratio of solution HF: HNO_3: H_2O = 1:4.5:4.5) was used to obtain a smooth surface. Subsequently, they were cleaned in acetone and ethanol, respectively, for 10 mins to remove organic solvent and dust, and finally dried in hot air.

The oxidation experiments were conducted with a simultaneous thermal analysis system (NETZSCH STA 449F) to acquire a continuous weight gain curve. The experimental procedure and parameter settings were similar to those used in our previous experiments [46]. The temperature of the samples rose to 1000 ℃ at a rate of 5 ℃/min, with inert gas (argon) flowing at 20 mL/min. As soon as the designated temperature was reached, water vapor at 150 ℃ was injected into the furnace and its flux was controlled at 50 mL/min. When the oxidation was completed, the water injection was shut down immediately to ensure the precision of oxidation time. Finally, the samples were cooled down in flowing argon. To follow different stages of oxidation, samples with three different oxidation times (as shown in Fig. 1) were chosen to prepare specimens for TEM observation. More detailed information is presented in Table 1.

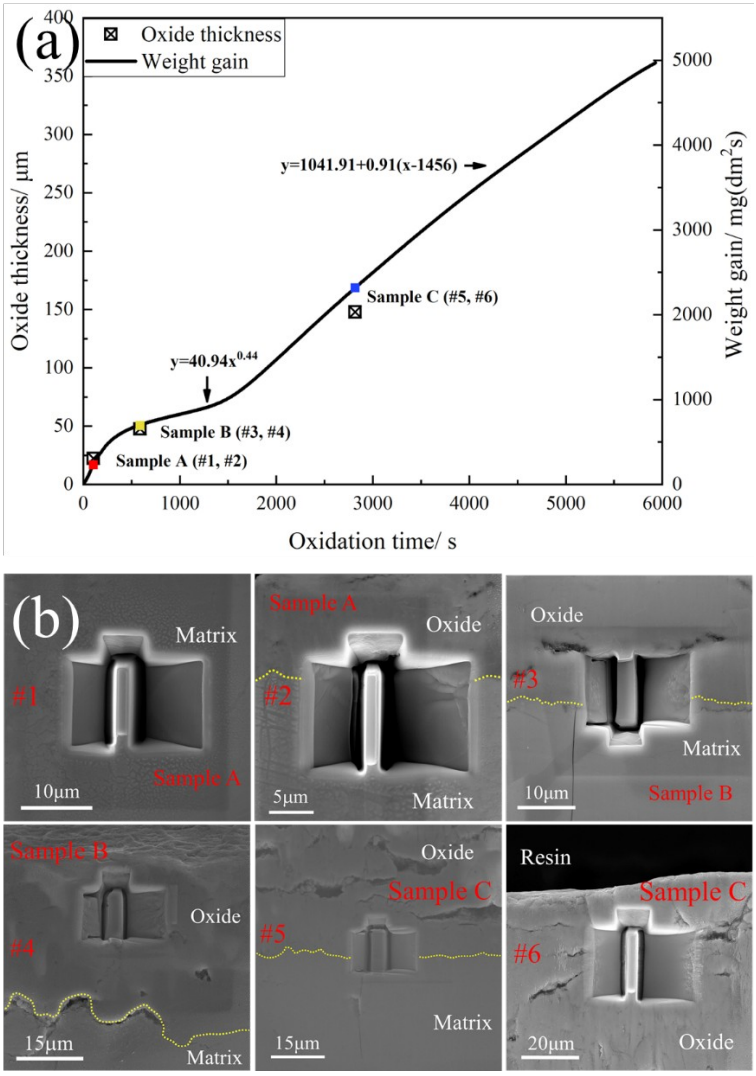

Fig. 1. Illustration of oxidation samples and TEM specimens (a) oxidation stages of three samples; (b) SEM SE images showing the location of TEM specimens

Table 1. The weight gain and oxide thickness of samples

Number	Oxidation time/ s	Weight gain/ mg · dm^{-2}	Oxide thickness/ μm
A	105	232.23	22.25
B	589	695.82	47.61
C	2818	2317.29	147.81

2.2 Microstructural characterization

After oxidation, a metallographic microscope (Axio Scope A1) was used to

obtain the overall morphology of the samples. To clearly observe matrix grains, acid pickling was performed on the sample A with the same acid solution mentioned above. The detailed microstructural information about the sample was obtained by TEM (FEI Tecnai F30) and ACTEM (FEI Themis Z) equipped with high-angle annular dark/bright field (HAADF/BF) detectors and energy dispersive spectroscopy (EDS) detectors. The porosity in oxide film was characterized using the scanning transformation electron microscopy (STEM) mode, showing a darker contrast due to the lower mass locally. Since particular attention was paid to the relationship between porosity and Zr-Sn intermetallic precipitates, which can be only observed in STEM mode, the contrast in STEM mode was considered as the criterion to identify nanovoids. The specimens used in the TEM experiments were prepared by focused ion beam technology (FIB, Thermo Scientific Scios 2), and foils with an approximated size of 4.5 μm × 4.5 μm × 50 nm were obtained. Six TEM specimens were extracted from different samples and different locations, as described in Fig. 1 and Table 2.

Table 2. Location and oxidation time of TEM samples

Number	Original sample	Oxidation time/s	Locations
#1	A	105	The core of matrix
#2	A	105	Matrix beneath the oxide film
#3	B	589	Inner side of oxide film
#4	B	589	Outer side of oxide film
#5	C	2818	Inner side of oxide film
#6	C	2818	Outer side of oxide film

In order to study the phase distribution at different scale thicknesses, S-XRD was conducted in the Shanghai Synchrotron Radiation Facility (SSRF). 2D SXRD measurements were conducted with the BL15U1 beamline and the obtained XRD patterns were recorded by a MAR-CCD 165 area detector as described in Fig. 2(a). The beam spot was approximately 3 (horizontal) × 0.5 (vertical) μm^2 at a wavelength

of 0.7293 Å, corresponding to a beam energy about 17.04 keV. This working energy is lower than zirconium K-edge absorption threshold and can thus avoid fluorescence effects [47]. The angle between incident beam and sample surface was fixed at 5°, which resulted in a penetration depth of about 11.7 μm. Before testing, the geometry of the experimental system was determined by calibrating with standard CeO_2 powder sample. To acquire the distribution of phases with respect to thickness, a scan along the oxidation direction throughout the whole cross section of the oxidized cladding tube was conducted with the step size of 1 μm, as shown in Fig. 2(b).

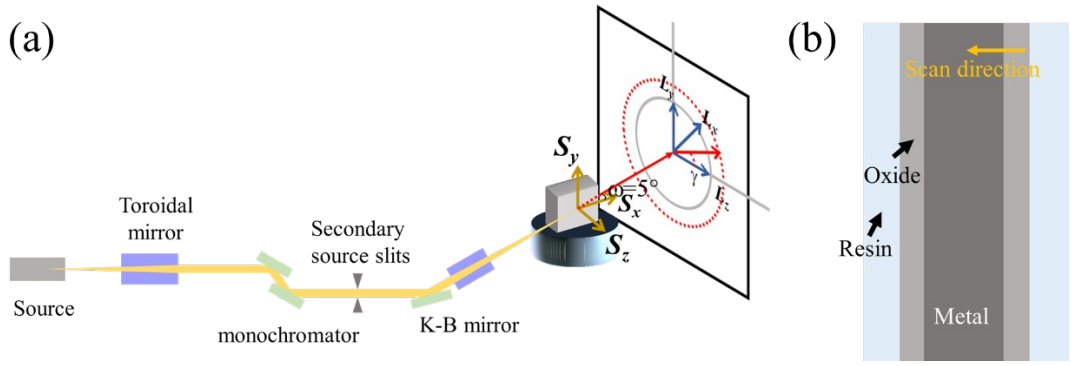

Fig. 2. (a) Schematic diagram of experimental equipment in SSRF; (b) scanning direction of S-XRD experiments

2.3 DFT simulation method

DFT simulations were performed using the Vienna ab initio simulation package (VASP) code [48–51]. The projector augmented-wave (PAW) method was employed for the description of ion-electron interactions, and the Perdew–Burke–Ernzerhof (PBE) functional was used to describe the electron-electron exchange correlations [52–54]. AIMD simulations were carried out using NVT ensemble with 300 eV energy cutoff of plane wave basis sets and 1 fs time step. And AIMD simulations were performed at 2000 K which is lower than the melting points of m-ZrO_2 and Zr_5Sn_3. The purpose of the AIMD simulation with small cutoff energy and high temperature is to achieve the relatively approximate structure relaxation. After AIMD simulations, DFT simulations with 500 eV cutoff energy were conducted to accurately optimize

atom positions, bringing about the findings that the system achieves the minimum total energy when the total energy changes between two steps are smaller than 10^{-5} eV and all the atomic forces are smaller than 0.02 eV $Å^{-1}$. It is noted that formation energies and atomic configurations are obtained by conventional DFT calculation at 0 K. For all DFT simulations and AIMD simulations present here, a single k-point was applied to perform the Brillouin zone. In this work, m-ZrO_2(001) with an O vacancy and perfect Zr_5Sn_3(100) interfaces were constructed to investigate the evolution of microstructure of Zr-Sn intermetallic phase and ZrO_2. The interface orientation of m-ZrO_2(001) (3×2)/Zr_5Sn_3(100) (2×2) was tailored to decrease the strain at the interface.

The formation energy E_f of O in bulk Zr_5Sn_3 was defined as:

$$E_f = E_{O+Zr_5Sn_3} - E_{Zr_5Sn_3} - \frac{1}{2}E_{O_2} \quad (1)$$

where $E_{O+Zr_5Sn_3}$ and $E_{Zr_5Sn_3}$ are the total energies of the supercell with and without O atom in bulk Zr_5Sn_3, respectively. E_{O_2} presents the total energy of an O_2 molecule in vacuum. For bulk Zr_5Sn_3, a 2 × 2 × 1 supercell was used and a 3 × 3 × 2 k-point mesh generated by the Monkhorst–Pack scheme was sampled in the first Brillouin zone [55]. To search for the minimum energy path (MEP) for O diffusion in bulk Zr_5Sn_3 [56], climbing image nudged elastic band (CI-NEB) was performed. Finally, MEP was achieved by five images between the initial state and the final state.

3. Results

3.1 Phase distribution

The phase distribution in the oxidized samples was characterized by SEM, metallographic microscope and S-XRD, as shown in Fig. 3. The SEM results of three samples in Fig. 3(a)-(c) show that the oxide film thickens with oxidation time. Since the Raman spectra in our previous research [46] have given the phase distribution in the oxide film, sample A with the biggest matrix area was chosen to perform further investigation through metallographic microscope and S-XRD. The metallographic

observations on sample A in Fig. 3(d) demonstrate that two distinct morphologies are observed in the matrix. The grains located in the core of matrix display the Widmanstatten morphology [57], which is similar to the parallel plate structure generated from β-α phase transformation during cooling [57]. In contrast to the matrix core, the grains beneath the oxide film are equiaxed, similar to α-Zr stabilized by oxygen [58,59], α-Zr(O). Due to the oxygen concentration gradient, α-Zr(O) only exists within a layer around 63 μm from the oxide-metal (O-M) interface. Meanwhile, Fig. 3(e) shows diffraction peaks obtained from integration of the whole 2-D diffraction pattern using S-XRD, respectively from the matrix and the oxide. In order to demonstrate the phase distribution of three layers observed by the metallographic microscope, the diffraction patterns were displayed with different steps. In the matrix, α-Zr is the dominant structure, which is characterized by three main peaks. Generally, increasing the temperature will cause α-β transformation of Zr [60,61]. However, the oxygen dissolved in the Zr lattice can preserve the structure of α-Zr, denoted as α-Zr(O), even at higher temperatures [62]. During the cooling, β-α transformation of Zr occurs and gives rise to the Widmanstatten morphology, different from the equiaxed structure observed before heating [57]. To distinguish two different morphologies of α-Zr, the term prior β-Zr was used to describe the α-Zr with Widmanstatten morphology, following previous work [5,63]. As for the oxide scale, it contains both the tetragonal and monoclinic phases. It can be seen that m-ZrO_2 dominates the oxide scale with a small proportion of t-ZrO_2. Based on the intensity of diffraction peaks, the t-ZrO_2 is distributed throughout the oxide film and its fraction gradually increases with thickness. The different metal grain morphologies with the same lattice structure result from the stabilization of α-Zr by temperature or by oxygen. Combining results from the two techniques, it can be concluded that, after cooling, samples display multiple layered structure, including prior β-Zr, α-Zr(O) and ZrO_2.

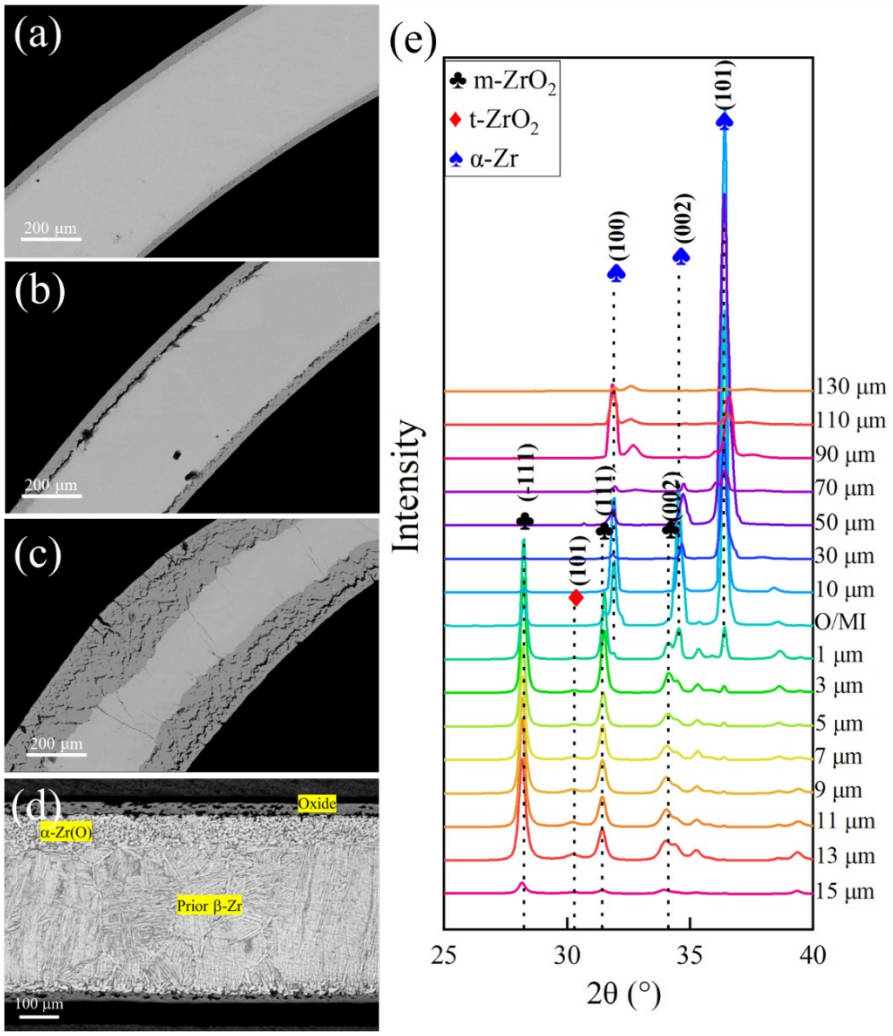

Fig. 3. SEM, metallographic microscope image and S-XRD results of the phase distribution in sample a: (a), (b) and (c) SEM SE images of sample A, B and C; (d) metallographic microscope results of sample A; (e) S-XRD scanning results of oxidation system.

3.2 Precipitates in the matrix and oxide

Particular attention has been paid to two alloying elements, Nb and Sn, and their precipitates. To gain a deep insight of the evolution of these particles, characterization results from three separate regions, prior β-Zr, α-Zr(O) and ZrO_2, were analyzed and compared.

3.2.1 precipitation in prior β-Zr and α-Zr(O)

Fig.4 displays the precipitation in the matrix, including both the prior β-Zr and α-Zr(O) layers. Sample A, with the biggest fraction of matrix, was used to prepare TEM specimens to characterize its microstructure. In the core of the matrix (specimen #1), in the layer of prior β-Zr, segregation of Nb with Fe enrichment on its edge was

observed, as shown in Fig. 4(a) and (b). Using selected area electron diffraction (SAED), Fig. 4(c) clearly shows that two phases are contained in the corresponding region, which were identified as α-Zr and β-Nb, respectively. The identification of the precipitation of Nb as β-Nb instead of β-Zr, which has a similar lattice parameter, is on the basis of their difference in oxidation resistance. β-Zr would be oxidized preferentially [64,65], while β-Nb can remain in the oxide because of the delayed oxidation of SPPs [14,66–68]. Since Nb precipitates in the oxide and matrix demonstrate a comparable size, it is assumed that the Nb precipitation in the matrix core is also β-Nb.

Similarly, Fig. 4(d) and (e) show that Nb-rich precipitates are located along the grain boundaries of α-Zr(O) in a TEM specimen extracted from sample A and denoted as specimen #2. Due to the linear morphology of Nb observed in the oxide film, as described in section 3.2.3, it is suggested that these Nb particles in the α-Zr(O) are preserved during oxidation. Therefore, the precipitation in α-Zr(O) layer is identified as β-Nb instead of β-Zr. In addition, it is noticeable that no segregation of Sn is observed in either α-Zr(O) or prior β-Zr.

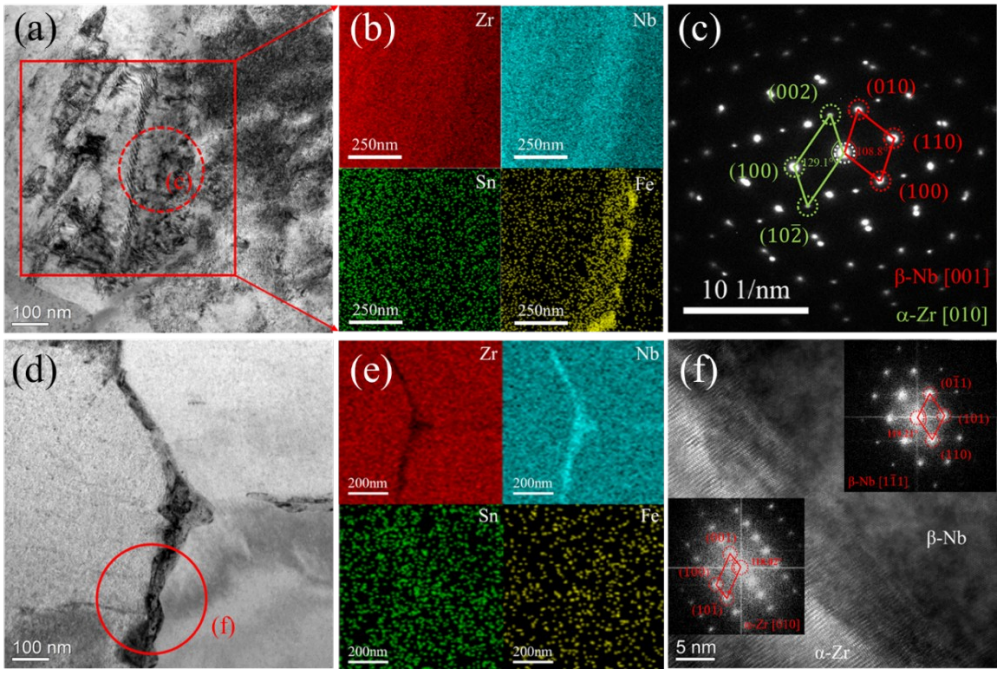

Fig. 4. TEM results from the matrix in sample A (oxidized for 105s): (a) BF image of β-Nb

precipitation in prior β-Zr (specimen #1); (b) EDS maps of Nb particles in prior β-Zr; (c) SAED result of Nb precipitation and matrix in prior β-Zr; (d) BF image of Nb particles in α-Zr(O) (specimen #2); (e) EDS maps of Nb particles in α-Zr(O); (f) HRTEM and corresponding FFT images of Nb particles and α-Zr(O)

3.2.2 The precipitation and concentration around the O-M interface

Fig. 5 demonstrates the precipitation and segregation of alloying elements around the O-M interface, characterized by TEM. Fig. 5(a) and (b) show a significant concentration of Sn near the O-M interface, accompanied by a moderate segregation of Nb. Through the EDS line scan result across the O-M interface in Fig. 5(c), the width of the Sn concentrated region around the O-M interface, is about 11 μm, and its location is marked according to the STEM result. The atomic concentration ratio of Sn to Zr in the Sn-concentrated area is in the range of 0.88 to 1.14. This kind of Sn concentration around the O-M interface is consistent with the APT results of Zircaloy corroded in 360 ˚C water [43], which reported segregation of Sn at the interface between ZrO and α-Zr(O). Wei et al. [2] also observed a segregation of Sn at the O-M interface after corrosion experiments at 360 ˚C with simulated primary water chemistry. However, in their opinion, this apparent segregation at the interface is attributed to the sensitivity of Sn to the evaporation field, and so is an APT evaporation artefact.

Also, around the O-M interface, a large number of small particles of Sn can be observed, as shown in Fig. 5(d). In the immediate vicinity of the O-M interface, small precipitates (around 10 nm, as shown in Fig. 5(e)) are dominant. The EDS maps in Fig. 5(f) demonstrate that they are Nb- and Sn-rich. Due to their small size, it is difficult to determine their structure. Besides, in the inner side of the oxide film, a linear β-Nb precipitate perpendicular to the O-M interface, as shown in Fig. 5(g) and Fig. 5(h), is also observed with a enrichment of Sn.

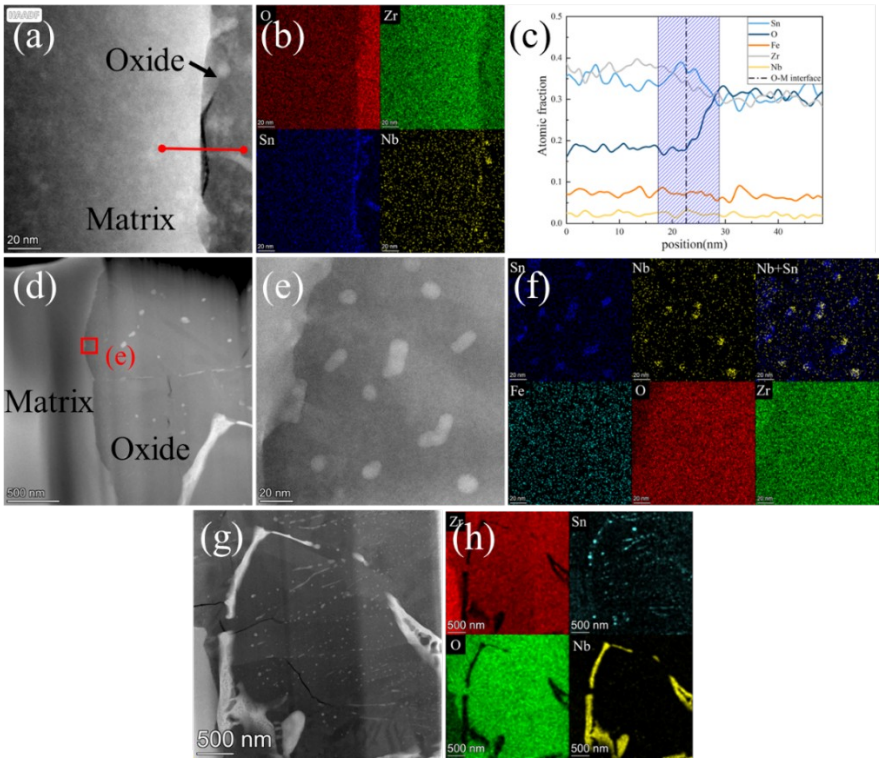

Fig. 5. Precipitation and segregation around O-M interface in the specimen #5: (a) HAADF image showing O-M interface morphology; (b) EDS maps from region shown in (a); (c) EDS line scan result from red line marked in (a); (d) HAADF image from region around the O-M interface; (e) HAADF image of area marked by red square in (d); (f) EDS maps of precipitation closed to the O-M interface; (g) Nb particles in the inner oxide film; (h) EDS maps of Nb particles in the inner scale

3.2.3 Precipitation in the oxide film

As the distance to the O-M interface increases, the precipitate size increases to up to 30 nm, while their density decreases dramatically. Fig. 6 shows the characterization results of these precipitates slightly further away from the O-M interface. Aiming to identify its structure, STEM-HAADF was used to characterize the larger precipitates in specimen #5. Fig. 6(a) and (b) present the HAADF image and EDS maps showing the Sn-rich precipitates. Its atomic arrangement was clearly obtained by STEM-HAADF, as shown in Fig.6 (c), further identified as Zr_5Sn_3. Due to the difference in atomic number (Zr=40, Sn=50), the Sn atoms appear brighter than Zr atoms (see Fig. 6(c)). The observation that Zr-Sn particles only exist in the oxide agrees with the ATP results obtained by Dong et al. [43]. They reported that Sn

segregation was only observed in the oxide, including ZrO and ZrO_2, with a lower Sn/Zr ratio in ZrO_2 than that in the suboxide. Other than linear β-Nb particles, Zr-Sn intermetallic particles always demonstrate a spherical morphology in the oxide.

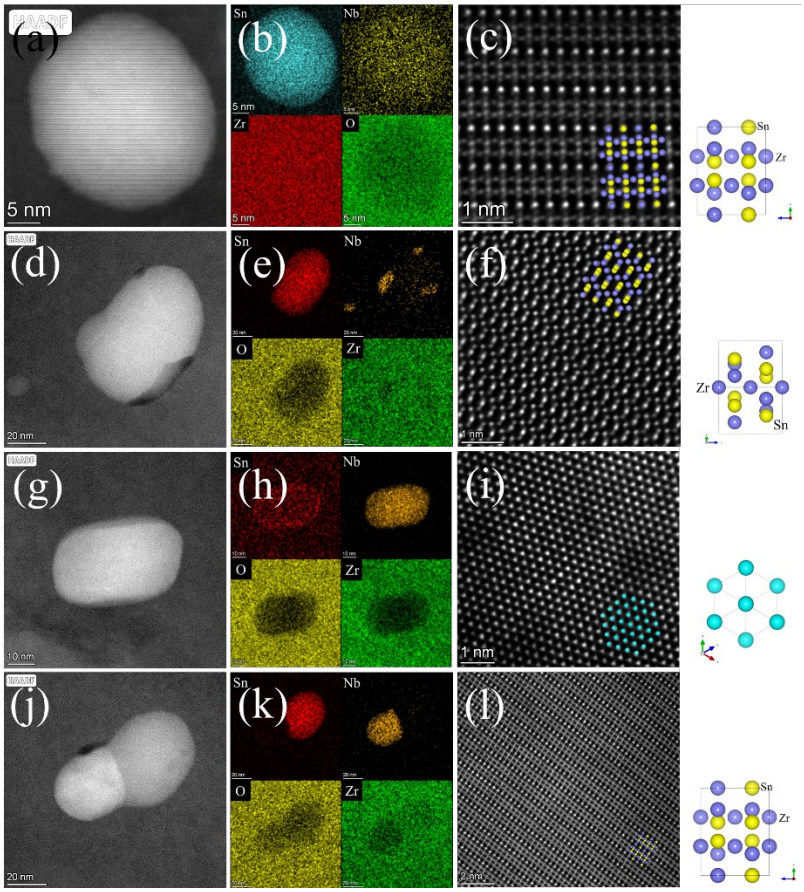

Fig. 6. Precipitation in the vicinity of the O-M interface in specimen #5 extracted from sample C (oxidized for 2818s): (a) HAADF image showing Zr_5Sn_3 precipitation; (b) EDS maps from (a); (c) HAADF atomic-resolution image from precipitate in (a); (d) HAADF image showing Zr_5Sn_3 precipitation; (e) EDS maps from (d); (f) HAADF atomic-resolution image from precipitate in (d); (g) HAADF image showing β-Nb particles; (h) EDS maps from (g); (i) HAADF atomic-resolution image from precipitate in (g); (j) HAADF image showing co-precipitation of Zr_5Sn_3 and β-Nb; (k) EDS maps from (j); (l) HAADF atomic-resolution image from precipitate in (j).

It should be noticed that a small concentration of Nb can be observed in the EDS maps of Zr_5Sn_3. To understand the co-precipitation of Nb and Sn, numerous TEM experiments were conducted for the Sn precipitates around the O-M interface, as shown in Fig. 6(d)-(n). The results can be classified into three categories:

(i) Zr_5Sn_3 surrounded by small Nb-rich regions, as shown in Fig. 6(d), (e) and (f);

(ii) β-Nb particles with segregated Sn at the interface, as shown in Fig. 6(j), (k) and

(l);

(iii) Closely associated Zr_5Sn_3 and the initially oxidized β-Nb particles, as shown in Fig. 6(g), (h) and (i);

These results do not demonstrate a clear precipitation sequence for the different phases incorporating these two elements. Unfortunately, the clear atomic arrangement of Nb particles cannot be obtained with the same zone axis of Zr_5Sn_3. However, according to the quantitative analysis of EDS spectrum, Nb particle makes a partial contribution to the local oxygen signal. Thus, it is suggested that Nb is slightly oxidized and embedded in ZrO_2 with metallic Zr_5Sn_3. It agrees with their oxidation sequence deduced from the standard Gibbs formation energies (per mole of O_2) of the oxides of Zr, Nb and Sn at 1000°C [69] (SnO: -318 kJ/mol, SnO_2: -317 kJ/mol, ZrO_2: -857.917 kJ/mol; NbO: -609.95 kJ/mol; NbO_2: -567.65 kJ/mol, Nb_2O_5: -539.53 kJ/mol).

3.3 Nanovoids in the oxide

To record the evolution of nanovoids during oxidation, STEM experiments were conducted at both the inner side (besides the O-M interface) and the outer side (close to the steam-oxide interface) of oxide films formed both before breakaway oxidation (sample B) and after breakaway oxidation (sample C). Before breakaway oxidation, several nanovoids are observed near the O-M interface (in Fig. 7(a)), while nanovoids at the outer side of scale in Fig. 7(b) display an obviously aligned tendency. After breakaway oxidation, a few microcracks are found in the vicinity of the O-M interface (as shown in Fig. 5(g)), whereas nanovoids are rarely observed along grain boudaries. As for the outer side of the oxide film, shown in Fig. 7(c), a multitude of interconnected nanovoids were observed, which results in the formation of microchannels along grain boundaries. Comparing Fig. 7(b) and (c), a significant increase in nanovoid density can be observed at the outer oxide film after the occurrence of breakaway oxidation. Furthermore, it should be noticed that precipitates are not observed in the outer side of the oxide film after breakaway oxidation.

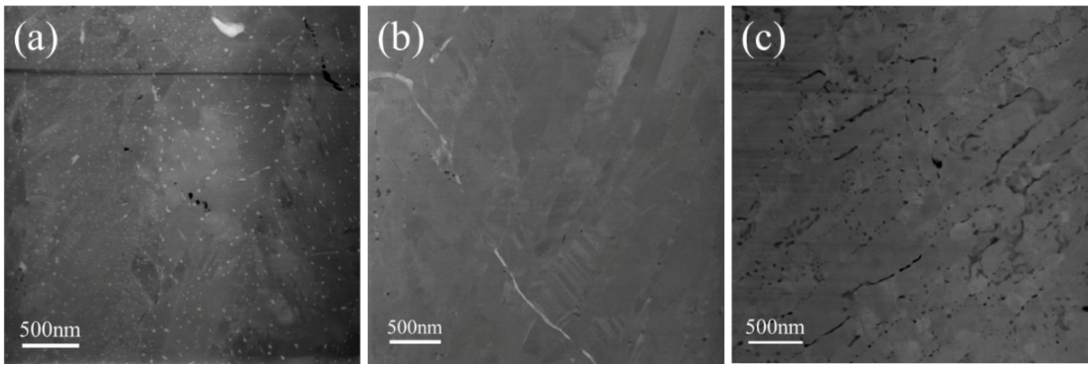

Fig. 7. HAADF images showing nanovoids in the oxide film: (a) the inner side of oxide film before breakaway oxidation (specimen #3); (b) the outer side of oxide film before breakaway oxidation (specimen #4); (c) the outer side of oxide film after breakaway oxidation (specimen #6)

Around the nanovoids at the outer side of an oxide film formed before breakaway oxidation occurs, a different intensity in the HAADF images is repeatedly observed (specimen #4), as shown in Fig. 8(a) and (b). EDS results in Fig. 8(c) imply that this interesting area beside the nanovoids is caused by a heterogeneous distribution of oxygen and tin. Using HAADF, an oxide region which exhibited a higher intensity (and, therefore, potentially a sub-stoichiometric oxide) was identified as ZrO, as shown in Fig. 8(d), while the area with a stronger contrast was identified as the monoclinic phase of ZrO_2, as shown in Fig. 8(e). The marked difference in atomic number result in the observation of only Zr in ZrO and ZrO_2. Due to the metastability of ZrO, quantitative EDS was performed in the oxygen-deficient area, obtaining a Zr:O ratio of ~1, suggesting that it is, indeed, ZrO. It also should be noted that a severe distortion occurs in the ZrO lattice, leading to a marked mismatch between the observed lattice structure and the ideal one. As for the Sn concentration, because of the small area of high Sn concentration, it is difficult to characterize its structure thoroughly. Combining the obtained STEM-HAADF results and the observation around the O-M interface, it is reasonable to believe that the residual Sn on the edge of nanovoids demonstrated in Fig. 8(g) is also a kind of Zr-Sn intermetallic phase, possibly Zr_5Sn_3. Measuring the interplanar spacing of Zr_5Sn_3 and ZrO obtained with fixed α and β angles in the TEM, it is suggested that ZrO compresses its lattice to

match the lattice parameter of Zr_5Sn_3 so that they can form an interface with lower energy, as shown in Fig. 8(h). Simultaneously, an area deficient in oxygen but with a significant Sn concentration can be observed next to the nanovoids, as shown in Fig. 8(i) and (j). Referring to the HAADF result in Fig.8(k), the suboxide is also identified as ZrO. Accordingly, it can be concluded that the region around nanovoids is composed of a composite structure, namely the nanovoid, Zr-Sn intermetallic phase, ZrO and ZrO_2.

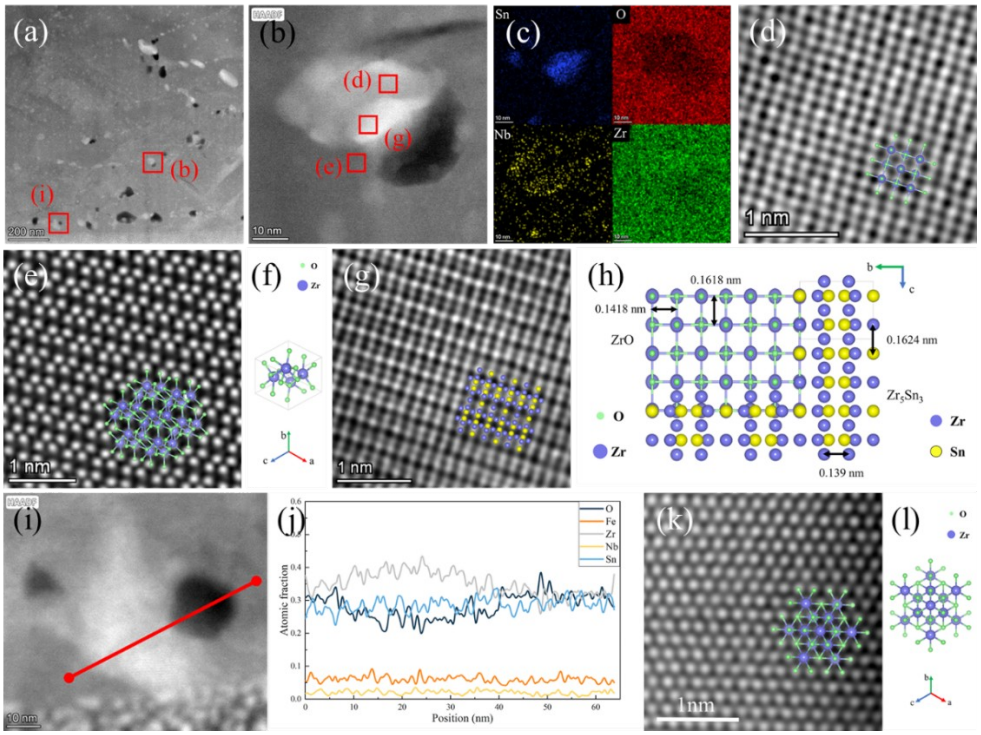

Fig. 8. Phase distribution around nanovoids: (a) HAADF image obtained at the outer side of oxide scale in specimen #4 (oxidized for 589s); (b) HAADF image showing nanovoids with Sn concentration; (c) EDS maps from the region shown in (b); (d) HAADF atomic-resolution image from ZrO; (e) HAADF atomic-resolution image from m-ZrO_2; (f) lattice structure of m-ZrO_2; (g) HAADF atomic-resolution image from Zr_5Sn_3; (h) the orientation relationship between ZrO and Zr_5Sn_3; (i) HAADF image showing nanovoids without Sn concentration; (j) EDS line scanning results of the red line in (i); (k) HAADF atomic-resolution image from the area deficient in oxygen; (l) lattice structure of m-ZrO_2.

3.4 DFT simulation

To study the evolution of Zr_5Sn_3 and provide an atomic-scale description of this process, AIMD and DFT simulations were used to track the trajectory of O, Zr and Sn

atoms at the ZrO_2/Zr_5Sn_3 interface. Fig. 9 shows the dynamic evolution of all atoms over the first 36 ps of simulation time for the ZrO_2/Zr_5Sn_3 interface. In order to analyze the results, dashed circles are employed to characterize the trajectories. Clearly, interdiffusion between Zr and Sn atoms has taken place at the interface. More specifically, O atoms at the interface tend to occupy octahedral interstitial positions of Zr in Zr_5Sn_3, which is mainly attributed to the low formation energy of O atoms (-5.17 eV) (see Fig. 10(a)). At 2 ps, the octahedral interstitial positions of Zr are wholly taken up with O atoms from the interface (black dotted circles in Fig. 9) leading to the formation of oxygen vacancies at the interface. On the other hand, this attraction between Zr and O atoms draws Zr atoms at the interface closer to the O atoms, causing larger spaces available for Sn and O atoms. It should be noted that Sn atoms at the interface without O are stabilized in the initial stages (blue dashed circle in Fig. 9). However, Sn atoms are observed to rearrange with the introduced O atoms by diffusion (red dashed circle in Fig. 9). In the following 3~36 ps, O atoms at the octahedral interstitial positions are not observed to further diffuse into Zr_5Sn_3, on account of the high diffusion barrier energy of 4.3 eV (see Fig. 10(b)), stabilizing at the interstitial positions. At 3 ps, Zr atoms from the subsurface diffuse to the interface assisted by O atoms. At 8 ps, Sn atoms at the interface migrate towards the subsurface. After 12 ps, the interdiffusion between a Zr atom from the subsurface and a Sn atom from the interface is completed, and the interdiffusion is stabilized at the interface subsequently (12~36 ps). Although the interdiffusion between two Zr and Sn atoms at the interface occurs at 28 ps, it then quickly returns to exchange between single Zr and Sn atoms.

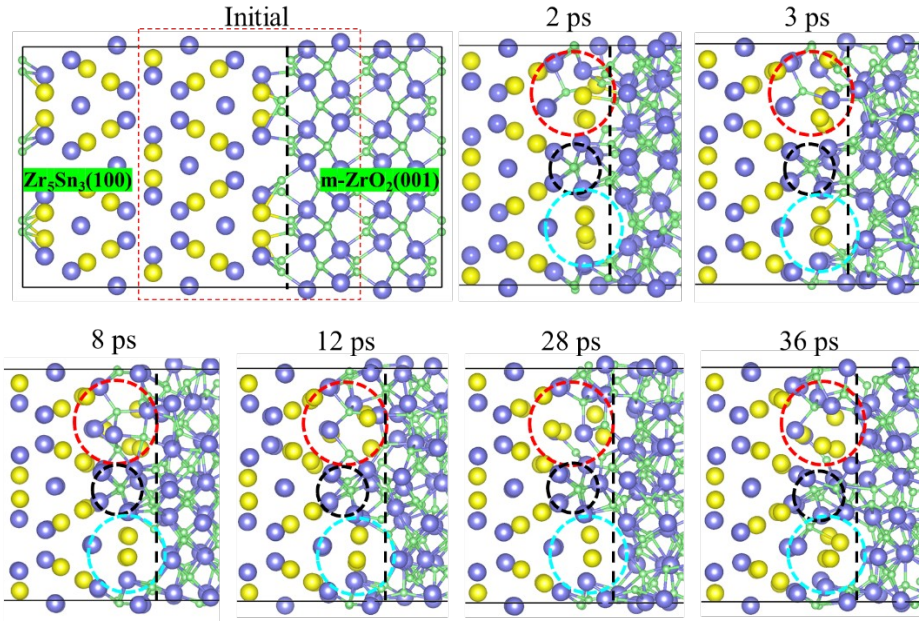

Fig. 9. Snapshots of the dynamic evolution at the ZrO_2/Zr_5Sn_3 interface. O, Sn and Zr atoms are colored with green, yellow and blue balls, respectively (similarly hereinafter).

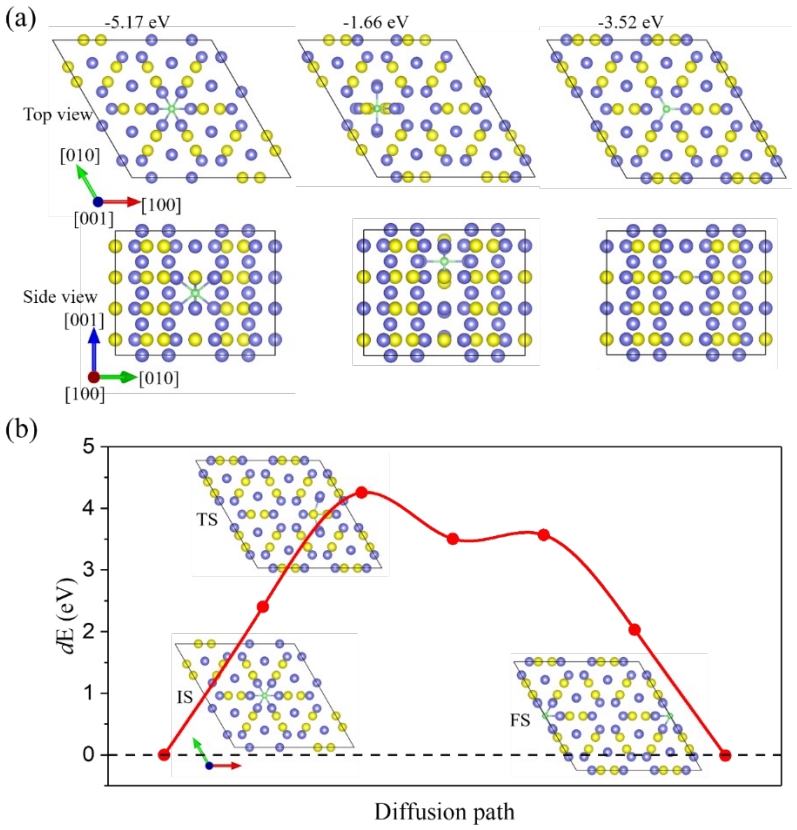

Fig. 10. Formation energy of interstitial O atoms and barrier energy of O diffusion in Zr_5Sn_3: (a) Top view and side top view of a single O in bulk Zr_5Sn_3 with corresponding formation energies of O at different interstitial sites; (b) Barrier energy of O diffusion in bulk Zr_5Sn_3 along with [100]

direction. The illustrations are the structures of initial state (IS), transition state (TS) and finial state (FS) in O diffusion from an octahedral interstitial position to another.

4. Discussion

4.1 The formation of Zr-Sn precipitate

As Arias and Roberti [8,12] reported, the solubility limit of Sn in α-Zr is about 1.2 at% at 853 K. Therefore, it could be expected that a complete Zr-Sn solid solution is formed in our experiments where the Sn content is 1 wt%. As such, the negative solution energy of Zr-Sn intermetallic phases calculated by DFT suggests that they tend to dissolve in the β-Zr phase [70]. Therefore, Sn particles are not observed in either the prior β-Zr layer or the α-Zr(O) layer. As we discussed before, Zr atoms will be preferentially oxidized, and, combining our EDS results, Sn atoms are repelled by the oxide and accumulate around the O-M interface, reaching a Sn/Zr concentration ratio around 1. With the assistance of temperature, this high concentration of Sn around O-M interface encourages the formation of Zr-Sn intermetallic phase according to the synthetic condition reported by previous research [71,72]. In addition, the high vacancy concentration generated at the O-M interface to balance the current of oxygen ion diffusion might also be beneficial to Zr-Sn intermetallic formation [73,74].

Based on the EDS maps and HAADF atomic-resolution image, it is concluded that Sn exists in the oxide in the form of Zr-Sn intermetallic precipitates, namely Zr_5Sn_3. Even though various Zr-Sn intermetallic phases were reported by Kwon and Crobett [45], according to previous DFT calculation results as listed in Table 3 [70,75], it is proposed that the most favorable Sn based intermetallic phase is Zr_5Sn_4, followed by Zr_5Sn_3. Both of these two phases belong to the Mn_5Si_3-type structure, and due to their structural resemblance [71,75,76], only a moderate enthalpy difference is expected in their formation. The limited Sn content in our materials cannot provide sufficient Sn atoms to serve as self-interstitials, thus leading to the formation of Zr_5Sn_3 instead of Zr_5Sn_4.

Table 3. The calculation results of Baykov et al. [75] Perez et al.[77] and Liu et al. [78]

Compound	Enthalpy of formation (meV/atom)		
	Baykov et al.	Pérez et al.	Liu et al.
Zr_4Sn	-29.940	-442.2	-309.0
Zr_3Sn	-34.834	-	-366.6
Zr_5Sn_3	-55.670	-770.5	-571.6
Zr_5Sn_4	-58.490	-820.0	-601.0
$ZrSn_2$	-42.905	-583.2	-443.8

To our knowledge, Zr-Sn intermetallic phases in the oxide film are rarely observed in corrosion experiments at 360 ˚C, but widely reported under the condition of neutron radiation at about 600 ˚C [79] or high-temperature steam oxidation [37–41]. This may result from the fact that growth of Zr-Sn intermetallic phase strongly depends on the temperature, leading to the all observations mentioned above being made under condition of enhanced Sn diffusion rate.

4.2 The formation of nanovoids and their influence on oxidation behavior

On the basis of the evolution and co-location of precipitates and nanovoids, it is logical to assume that their formation correlates to the Zr-Sn particles. According to our simulation results, Sn atoms in Zr_5Sn_3 tend to diffuse into oxide, which is a process commonly observed during the oxidation of SPPs. When the SPPs oxidize, the alloying element would migrate out the original SPP bounds [80]. Thus, it is suggested that the diffusion of Sn from Zr_5Sn_3 to the ZrO_2 also accompany the oxidation of Sn element.

Combining our simulation and experimental results, a mechanism about the evolution from Zr_5Sn_3 precipitates to nanovoids can be proposed illustrated by the schematic in Fig. 11. According to our DFT and AIMD simulations, Sn atoms in the Zr-Sn intermetallic phase tend to diffuse toward zirconia, while oxygen atoms in the oxide are inclined to move in the opposite direction. As a result, the moving oxygen atoms combine with Zr atoms in the precipitates forming oxide. Due to the moderate oxidation rate before breakaway oxidation, the oxidation interaction gives rise to ZrO

next to the nanovoids. Regions deficient in oxygen were not observed after breakaway oxidation, as shown in Fig. 7(c). It is then assumed that the suboxide next to nanovoids is completely oxidized after long-term oxidation. As for Sn atoms, their slow migration in the oxide also accompanies the oxidation. which means Sn chemical potential varies during the diffusion, as suggested by Bell [32]. At the beginning of oxidation, to achieve lower energy and stabilize themselves, Sn atoms with +2 state would capture oxygen vacancies in the oxide film to form the bound defect $\{Sn_{Zr}:V_O\}$. As oxidation of Sn proceeds, the valence state transformation from +2 to +4 results in isolated Sn ions dissolved in zirconia. The remaining vacancies would be captured by the interface between precipitates and zirconia, and aggregates of vacancies will finally form isolated aligned nanovoids in grains or along grain boundaries. On the basis of this mechanism, the distribution of Zr-Sn precipitates could be considered as the explanation for the aligned nanovoids observed after breakaway oxidation. It can also provide an explanation for the uniform distribution of component around the nanovoids. When the Zr_5Sn_3 is partly consumed, nanovoids, a high local concentration of Sn and an area deficient in oxygen coexist, as shown in Fig. 8(b). When the Zr-Sn precipitate is completely depleted, nanovoids surrounded by an area deficient in oxygen can be observed, as displayed in Fig. 8(i). After breakaway oxidation, the accelerating oxidation rate and prolonged oxidation time cannot maintain the suboxide around the nanovoids, which then gives rise to the isolated nanovoids. It should be noted that, in general, stress relaxation caused by the t-m transformation of ZrO_2 is the accepted reason for porosity in oxide film [23,81]. However, as reported by Idarraga et al [36], t-ZrO_2 becomes more difficult to observe at higher temperatures, so it seems likely that the impact of t-m transformation in the oxide film will also weaken, and that the effect of Zr-Sn precipitation may play a more dominant role. At the higher temperature where the existence of Zr-Sn intermetallic phases has been confirmed, it is believed that the mechanism is valid. For the service condition, even though the Sn segregation [43] and nanovoids [82] were observed in the oxide separately, the relationship between them has not been

proposed yet. Thus, we suggest that further investigation on the existence of Zr-Sn phase is required before applying the mechanism to lower temperature.

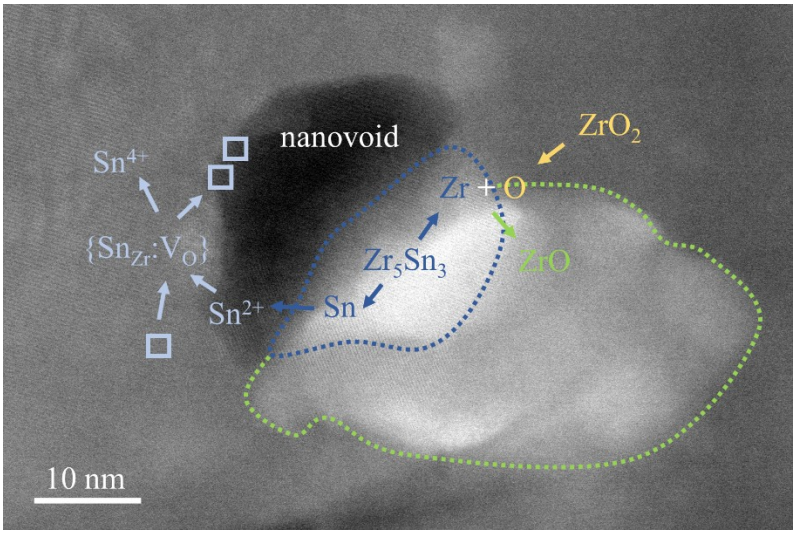

Fig. 11. Schematic diagram of the formation of the nanovoids

After prolonged oxidation, nanovoids both in grains and at the grain boundaries are gradually formed and connect with each other, which ultimately constitutes microchannels in Fig. 7(c) through the oxide, as described by Fig. 12. As previous characterization has shown, a preferential orientation of oxide growth induces the formation of columnar oxide grains with a strong fiber texture perpendicular to the O-M interface [83,84]. Correspondingly, the microchannels deriving from connected nanovoids located at the grain boundaries also develop perpendicular to the O-M interface, which is along the diffusion direction of oxygen. Serving as easy path for oxygen diffusion, the microchannels necessarily accelerate the oxidation as described in previous research [14,36,46,82]. When reaching the inner side of the oxide film, these microchannels would trigger the occurrence of breakaway oxidation. As the Sn content increases, the densities of both Zr-Sn particles and nanovoids deriving from Zr-Sn precipitation increase. It can be inferred that the distance between nanovoids would also decrease, leading to the easier formation of microchannels and earlier occurrence of breakaway oxidation as reported by Wei et al. [2]. Indeed, the formation of nanovoids deriving from Zr-Sn precipitation can be considered as the result of the

oxidation of tin, thus the transformation from Zr-Sn intermetallic precipitates to nanovoids requires a particular oxidation time. In this case, the aligned nanovoids are gradually formed in the oxide with a certain distance away from the O-M interface, which means there is a constant thickness of dense inner side. Therefore, a linear oxidation kinetics can be observed after breakaway oxidation due to this dense layer with constant thickness, as proposed by Maroto et al. [85]. However, it is noteworthy that the breakaway oxidation with linear oxidation kinetics [65,86] and connected nanovoids [82] were also found in zirconium alloy containing no Sn. Therefore, it is suggested that mechanism proposed in the present work explains the influence of Sn on oxidation resistance, but further research is still required to find out the underlying mechanisms behind the initiation of microchannels in other cases.

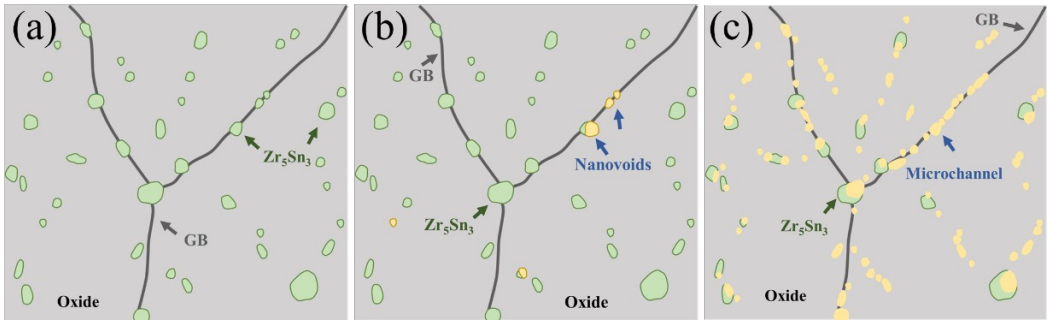

Fig. 12. Schematic diagram of the effect of Sn on the oxidation behavior through Zr-Sn intermetallic phase and nanovoids.

4.3 The co-precipitation of Sn and Nb and its influence on oxidation behavior

According to the three types of co-precipitation of Sn and Nb shown in Fig. 6, it is difficult to draw a conclusion on the sequence of their formation. After all, Zr_5Sn_3 with Nb segregation on its edge and β-Nb with an edge segregated with Sn can be observed simultaneously. More importantly, neither isolated Nb precipitation nor isolated Sn segregation was found in the vicinity of the O-M interface. On the basis of atomic volume, the compression induced by Nb atoms in the Zr lattice can be compensated by the larger Sn atoms. This compensation leads to a drop in strain energy and stabilizes the system, which is supported by the optimal distance between Sn and Nb atoms given by Wu et al. based on mixing energy and Nb-Sn binding

energy by DFT simulations [87]. Therefore, the conclusion that Sn and Nb attract each other and can precipitate to form a number of different phases in close proximity rather than precipitating following a specific sequence, can be drawn. This concentration feature of Nb and Sn is still valid when Sn accumulated around the interface and react with Zr to form Zr-Sn clusters and when linear β-Nb formed in the matrix. It means that when Zr-Sn clusters are included into the oxide film, there are a range of Nb clusters surrounding them, which would then lead to the co-precipitation of Nb and Sn phases. Analogously, linear β-Nb particles formed in the matrix, due to the solubility change of Nb during the β-α transformation of Zr [88,89], also attract Zr-Sn clusters formed around the O-M interface contributing to the co-precipitation shown in Fig. 5(h).

It is commonly believed that dispersed β-Nb particles can improve the oxidation resistance by relaxation of accumulated stress during oxidation, which stabilizes the columnar grains and reduce the possibility of cracks under operating condition [81,90]. However, for the higher temperature, the mechanism proposed in present work suggests that the addition of Nb in the Zr-Sn-Nb alloy system would cause a higher density of co-precipitation resulting in easier connection between nanovoids deriving from Zr_5Sn_3. Meanwhile, the linear β-Nb particles formed at α-Zr(O) likewise attract Zr-Sn clusters, resulting in Zr-Sn precipitates embedded in linear β-Nb particles, as shown in Fig. 5(h), and connected nanovoids along the oxidation direction. Referring to this mechanism, it is suggested that the improvement of oxidation behavior of the Zr-Sn-Nb alloy system can be achieved by an appropriate decrease of Sn content, so that the density of nanovoids can be controlled to be low enough to impede the formation of microchannels while preserving the improvements in mechanical properties induced by the inclusion of Sn. Also, the co-precipitation mechanism may provide an explanation for the different oxidation resistance observed between Zr-Nb and Zr-Sn-Nb alloy systems caused by the addition of Sn [2,86,91].

5. Conclusion

A study on oxidation behavior in high-temperature steam at 1000 ℃ was carried out using STA, metallographic microscope, S-XRD, TEM and ACTEM. Combining the simulation and experimental results, a new standpoint to understand the role of Sn element is provided referring to the Zr-Sn intermetallic precipitates and nanovoids. Several conclusions are drawn as below:

(1) During oxidation, Sn atoms dissolving in matrix are rejected by the oxide and accumulate around the O-M interface and form Zr-Sn intermetallic precipitates, which were identified as Zr_5Sn_3, in the oxide.

(2) The AIMD and DFT simulations show that there is a tendency that O atoms in the ZrO_2 will diffuse toward to Zr-Sn particles, forming Zr_xO_y compound and are stabilized at the octahedral interstitial positions. Zr atoms at the ZrO_2/Zr_5Sn_3 interface prefer to permeate into the Zr-Sn particles, assisted by O atoms. But Sn atoms in the Zr-Sn particles are inclined to migrate along the opposite direction of the migrating O atoms.

(3) Due to the oxidation and diffusion of Sn atoms in the Zr-Sn precipitates, nanovoids are formed adjacent to the Zr-Sn particles. The vacancies left by transformation from Sn^{2+} to Sn^{4+} segregate at the interface between precipitates and the oxide and eventually form nanovoids. Meanwhile, the movement of O atoms would lead to a local area deficient in oxygen next to the nanovoids.

(4) As oxidation proceeds, isolated nanovoids along grain boundaries would connect with each other and lead to the formation of microchannels perpendicular to the O-M interface. These microchannels provide easy diffusion paths for oxygen, which inevitably causes oxidation acceleration, that is, breakaway oxidation. Correspondingly, the co-precipitation of Nb and Sn induces a higher density of nanovoids and easier formation of microchannels, which can be considered as a new route to understand the role of Sn in the oxidation of Zr-Sn-Nb alloy systems.

Acknowledgements

Financial support provided by the National Science and Technology Major Project

(No. 2017ZX06002004), China Scholarship Council (No. 201906280379). We thank Dr. Sheng Jiang at SSRF for his support in the S-XRD experiments. Also, we sincerely appreciate the advisory input of Professor Chris R.M. Grovenor at University of Oxford and the discussion on matrix with Dr. Guanze He at University of Oxford.

Data availability

The raw/processed data required to reproduce these findings cannot be shared at this time as the data also forms part of an ongoing study.

Reference

[1] H.-G. Kim, I.-H. Kim, B.-K. Choi, J.-Y. Park, A study of the breakaway oxidation behavior of zirconium cladding materials, Journal of Nuclear Materials 418 (n.d.) 186–197. https://doi.org/10.1016/j.jnucmat.2011.06.039.

[2] J. Wei, P. Frankel, E. Polatidis, M. Blat, A. Ambard, R.J. Comstock, L. Hallstadius, D. Hudson, G.D.W. Smith, C.R.M. Grovenor, M. Klaus, R.A. Cottis, S. Lyon, M. Preuss, The effect of Sn on autoclave corrosion performance and corrosion mechanisms in Zr-Sn-Nb alloys, Acta Mater 61 (2013) 4200–4214. https://doi.org/10.1016/j.actamat.2013.03.046.

[3] J.L. Vandegrift, P.M. Price, J.P. Stroud, C.J. Parga, I.J. Van Rooyen, B.J. Jaques, D.P. Butt, Oxidation behavior of Zirconium, Zircaloy-3, Zircaloy-4, Zr-1Nb, and Zr-2.5Nb in air and oxygen, Nuclear Materials and Energy 20 (2019). https://doi.org/10.1016/j.nme.2019.100692.

[4] M. Steinbrück, M. Böttcher, Air oxidation of Zircaloy-4, M5® and ZIRLO™ cladding alloys at high temperatures, in: Journal of Nuclear Materials, 2011: pp. 276–285. https://doi.org/10.1016/j.jnucmat.2011.04.012.

[5] H. Hoon Kim, J. Ho Kim, J. Young Moon, H. Seong Lee, J. Joo Kim, Y. Suck Chai, High-temperature Oxidation Behavior of Zircaloy-4 and Zirlo in Steam Ambient, 2010.

[6] J. Böhmert, M. Dietrich, J. Linek, Comparative studies on high-temperature corrosion of ZrNb1 and Zircaloy-4, Nuclear Engineering and Design 147 (1994) 53–62. https://doi.org/10.1016/0029-5493(94)90256-9.

[7] P. Bossis, B. Verhaeghe, S. Doriot, D. Gilbon, V. Chabretou, A. Dalmais, J.-P. Mardon, M. Blat, A. Miquet, In PWR comprehensive study of high burn-up corrosion and growth behavior of M5® and recrystallized low-tin Zircaloy-4, in: Zirconium in the Nuclear Industry: 15th International Symposium, ASTM International, 2009.

[8] H. Yang, J. Shen, Y. Matsukawa, Y. Satoh, S. Kano, Z. Zhao, Y. Li, F. Li, H. Abe, Effects of alloying elements (Sn, Nb, Cr, and Mo) on the microstructure and

mechanical properties of zirconium alloys, J Nucl Sci Technol 52 (2015) 1162–1173. https://doi.org/10.1080/00223131.2014.996622.
[9] S.Y. Lee, K.T. Kim, S.I. Hong, Circumferential creep properties of stress-relieved Zircaloy-4 and Zr–Nb–Sn–Fe cladding tubes, Journal of Nuclear Materials 392 (n.d.) 63–69. https://doi.org/10.1016/j.jnucmat.2009.03.045.
[10] A.M. Garde, S.R. Pati, M.A. Krammen, G.P. Smith, R.K. Endter, Corrosion behavior of Zircaloy-4 cladding with varying tin content in high-temperature pressurized water reactors, ASTM, Philadelphia, PA (United States), 1994.
[11] K. Takeda, H. Anada, Mechanism of corrosion rate degradation due to tin, in: Zirconium in the Nuclear Industry: Twelfth International Symposium, ASTM International, 2000: pp. 592–608.
[12] D. Arias, L. Roberti, The solubility of tin in α and β zirconium below 1000°C, Journal of Nuclear Materials 118 (1983) 143–149. https://doi.org/10.1016/0022-3115(83)90219-2.
[13] J.-Y. Park, B.-K. Choi, S.J. Yoo, Y.H. Jeong, Corrosion behavior and oxide properties of Zr–1.1 wt%Nb–0.05 wt%Cu alloy, Journal of Nuclear Materials 359 (n.d.) 59–68. https://doi.org/10.1016/j.jnucmat.2006.07.017.
[14] J. Huang, M. Yao, C. Gao, X. Liang, J. Peng, J. Zhang, B. Zhou, The influence of second phase particles on the crack formation in oxide films formed on zirconium alloys, Corros Sci 99 (2015) 172–177. https://doi.org/10.1016/j.corsci.2015.06.030.
[15] H.-G. Kim, J.-Y. Park, Y.-H. Jeong, Ex-reactor corrosion and oxide characteristics of Zr–Nb–Fe alloys with the Nb/Fe ratio, Journal of Nuclear Materials 345 (n.d.) 1–10. https://doi.org/10.1016/j.jnucmat.2005.04.061.
[16] J.-Y. Park, B.-K. Choi, S.J. Yoo, Y.H. Jeong, Corrosion and oxide properties of HANA alloys, J ASTM Int 5 (2008) 1–13.
[17] H. Anada, K. Takeda, Microstructure of Oxides on Zircaloy-4, 1.0Nb Zircaloy-4, and Zircaloy-2 Formed in 10.3-MPa Steam at 673 K, (1996).
[18] Y. Ding, D.O. Northwood, Tem study of the oxide-metal interface formed during corrosion of Zr-2.5wt.%Nb pressure tubing, Mater Charact 30 (1993) 13–22. https://doi.org/10.1016/1044-5803(93)90004-F.
[19] J.S. Moya, M. Diaz, J.F. Bartolome, Zirconium oxide film formation on zircaloy by water corrosion, Acta Mater 48 (2000) 4749–4754.
[20] R.C. Garvie, Stabilization of the tetragonal structure in zirconia microcrystals, Journal of Physical Chemistry 82 (1978) 218–224. https://doi.org/10.1021/j100491a016.
[21] W. Qin, C. Nam, H.L. Li, J.A. Szpunar, Tetragonal phase stability in ZrO2 film formed on zirconium alloys and its effects on corrosion resistance, Acta Mater 55 (2007) 1695–1701. https://doi.org/10.1016/j.actamat.2006.10.030.
[22] L. Kurpaska, J. Favergeon, L. Lahoche, G. Moulin, M. El Marssi, J.M. Roelandt, Zirconia layer formed by high temperature oxidation of pure zirconium: Stress generated at the zirconium/zirconia interface, Oxidation of Metals 79 (2013) 261–277. https://doi.org/10.1007/s11085-012-9348-9.
[23] D.J. Park, J.Y. Park, Y.H. Jeong, J.Y. Lee, Microstructural characterization of ZrO2

layers formed during the transition to breakaway oxidation, Journal of Nuclear Materials 399 (2010) 208–211. https://doi.org/10.1016/j.jnucmat.2010.01.021.
[24] E. Polatidis, P. Frankel, J. Wei, M. Klaus, R.J. Comstock, A. Ambard, S. Lyon, R.A. Cottis, M. Preuss, Residual stresses and tetragonal phase fraction characterisation of corrosion tested Zircaloy-4 using energy dispersive synchrotron X-ray diffraction, Journal of Nuclear Materials 432 (2013) 102–112. https://doi.org/https://doi.org/10.1016/j.jnucmat.2012.07.025.
[25] P. Li, I.-W. Chen, J.E. Penner-Hahn, Effect of Dopants on Zirconia Stabilization-An X-ray Absorption Study: I, Trivalent Dopants, Journal of the American Ceramic Society 77 (n.d.) 118–128. https://doi.org/10.1111/j.1151-2916.1994.tb06964.x.
[26] P. Ghigna, G. Spinolo, U. Anselmi-Tamburini, F. Maglia, M. Dapiaggi, G. Spina, L. Cianchi, Fe-Doped Zirconium Oxide Produced by Self-Sustained High-Temperature Synthesis: Evidence for an Fe−Zr Direct Bond, J Am Chem Soc 121 (n.d.) 301–307. https://doi.org/10.1021/ja982335a.
[27] S. Fabris, A.T. Paxton, M.W. Finnis, A stabilization mechanism of zirconia based on oxygen vacancies only, Acta Mater 50 (2002) 5171–5178. https://doi.org/10.1016/S1359-6454(02)00385-3.
[28] X. Guo, T. Schober, Water Incorporation in Tetragonal Zirconia, Journal of the American Ceramic Society 87 (n.d.) 746–748. https://doi.org/10.1111/j.1551-2916.2004.00746.x.
[29] S. Shukla, S. Seal, Mechanisms of room temperature metastable tetragonal phase stabilisation in zirconia, International Materials Reviews 50 (n.d.) 45–64. https://doi.org/10.2279/174328005X14267.
[30] S. Leistikow, EXPOSED TO HIGH TEMPERATURE STEAM AND HYDROGEN-STEAM MIXTURES, (1987).
[31] S. Leistikow, S.G. Schanz, The oxidation behavior of Zircaloy-4 in steam between 600 and 1600°C, Materials and Corrosion 36 (1985) 105–116. https://doi.org/10.1002/maco.19850360302.
[32] B.D.C. Bell, S.T. Murphy, P.A. Burr, R.W. Grimes, M.R. Wenman, Accommodation of tin in tetragonal ZrO2, J Appl Phys 117 (2015). https://doi.org/10.1063/1.4909505.
[33] B.D.C. Bell, S.T. Murphy, R.W. Grimes, M.R. Wenman, The effect of Sn–VO defect clustering on Zr alloy corrosion, Corros Sci 141 (2018) 14–17. https://doi.org/10.1016/j.corsci.2018.06.020.
[34] J.L. Vandegrift, P.M. Price, J.-P. Stroud, C.J. Parga, I.J. Van Rooyen, B.J. Jaques, D.P. Butt, Oxidation behavior of Zirconium, Zircaloy-3, Zircaloy-4, Zr-1Nb, and Zr-2.5Nb in air and oxygen, (2019). https://doi.org/10.1016/j.nme.2019.100692.
[35] M. Steinbrueck, M. Boettcher, Air oxidation of Zircaloy-4, M5® and ZIRLO™ cladding alloys at high temperatures, Journal of Nuclear Materials 414 (2011) 276–285. https://doi.org/10.1016/j.jnucmat.2011.04.012.
[36] I. Idarraga, M. Mermoux, C. Duriez, A. Crisci, J.P. Mardon, Raman investigation of pre- and post-breakaway oxide scales formed on Zircaloy-4 and M5® in air

at high temperature, Journal of Nuclear Materials 421 (2012) 160–171. https://doi.org/10.1016/j.jnucmat.2011.11.071.
[37] C.M. Lee, D.-S. Sohn, Enhanced high-temperature oxidation resistance of a zirconium alloy cladding by high-temperature preformed oxide on the cladding, Corros Sci 131 (n.d.) 116–125. https://doi.org/10.1016/j.corsci.2017.11.019.
[38] M. Grosse, R. Simon, Analysis of tin diffusion in Zircaloy-4 and tin redistribution after steam oxidation by means of X-ray fluorescence measurements, Adv Eng Mater 11 (2009) 483–487. https://doi.org/10.1002/adem.200800344.
[39] J.H. Back, K.B. Park, Y.H. Jeong, Oxidation kinetics of Zircaloy-4 and Zr-1Nb-1Sn-0.1Fe at temperatures of 700-1200°C, Journal of Nuclear Materials 335 (2004) 443–456. https://doi.org/10.1016/j.jnucmat.2004.08.007.
[40] R.E. Pawel, R.A. Perkins, R.A. McKee, J. V Cathcart, G. Yurek, R. Druschel, Diffusion of oxygen in beta-zircaloy and the high temperature zircaloy-steam reaction, Zirconium in the Nuclear Industry, ASTM STP 633 (1977) 119–133.
[41] W.G. Dobson, R.R. Biederman, R.G. Ballinger, Zircaloy-4 oxidation in steam under transient oxidizing conditions, in: Zirconium in the Nuclear Industry, ASTM International, 1977.
[42] G.J.C. Carpenter, E.F. Ibrahim, J.F. Watters, The aging response of zirconium-tin alloys, Journal of Nuclear Materials 102 (n.d.) 280–291. https://doi.org/10.1016/0022-3115(81)90495-5.
[43] Y. Dong, A.T. Motta, E.A. Marquis, Atom probe tomography study of alloying element distributions in Zr alloys and their oxides, Journal of Nuclear Materials 442 (2013) 270–281. https://doi.org/10.1016/j.jnucmat.2013.08.055.
[44] R. Yuan, Y.P. Xie, T. Li, C.H. Xu, M.Y. Yao, J.X. Xu, H.B. Guo, B.X. Zhou, An origin of corrosion resistance changes of Zr alloys: effects of Sn and Nb on grain boundary strength of surface oxide, Acta Mater 209 (2021). https://doi.org/10.1016/j.actamat.2021.116804.
[45] Y. Uk Kwon, J. D. Corbett, The zirconium-tin system, with particular attention to the Zr5Sn3-Zr5Sn4 region and Zr4Sn, Chemistry of Materials 2 (2002) 27–33. https://doi.org/10.1021/cm00007a005.
[46] Z. Cui, J. Liu, P. Hu, J. Qiu, S. Xie, R. Meng, W. Liu, G. Bai, D. He, D. Yun, Role of microchannels in breakaway oxidation of Zr alloy under high-temperature steam oxidation at 1000 ℃, Corros Sci 199 (2022) 110204. https://doi.org/10.1016/j.corsci.2022.110204.
[47] R. Guillou, M. Le Saux, E. Rouesne, D. Hamon, C. Toffolon-Masclet, D. Menut, J.C. Brachet, J.L. Béchade, D. Thiaudière, In-situ time-resolved study of structural evolutions in a zirconium alloy during high temperature oxidation and cooling, Mater Charact 158 (n.d.) 109971. https://doi.org/10.1016/j.matchar.2019.109971.
[48] R.O. Jones, O. Gunnarsson, The density functional formalism, its applications and prospects, Rev Mod Phys 61 (n.d.) 689–746. https://doi.org/10.1103/RevModPhys.61.689.

[49] W. Kohn, L.J. Sham, Self-consistent equations including exchange and correlation effects, Physical Review 140 (n.d.) A1133–A1138. https://doi.org/10.1103/PhysRev.140.A1133.
[50] G. Kresse, J. Furthmüller, Efficient iterative schemes for ab initio total-energy calculations using a plane-wave basis set, Phys Rev B Condens Matter 54 (n.d.) 11169–11186. https://doi.org/10.1103/PhysRevB.54.11169.
[51] G. Kresse, J. Hafner, Ab initio molecular dynamics for open-shell transition metals, Phys Rev B Condens Matter 48 (n.d.) 13115–13118. https://doi.org/10.1103/PhysRevB.48.13115.
[52] J. Perdew, K. Burke, M. Ernzerhof, Generalized gradient approximation made simple (vol 77, pg 3865, 1996), Phys Rev Lett 78 (n.d.) 1396–1396. https://doi.org/10.1103/PhysRevLett.78.1396.
[53] P.E. Blöchl, Projector augmented-wave method, Phys Rev B Condens Matter 50 (n.d.) 17953–17979. https://doi.org/10.1103/PhysRevB.50.17953.
[54] G. Kresse, D. Joubert, From ultrasoft pseudopotentials to the projector augmented-wave method, Phys Rev B Condens Matter Mater Phys 59 (1999) 1758–1775. https://doi.org/10.1103/PhysRevB.59.1758.
[55] H.J. Monkhorst, J.D. Pack, Special points for Brillouin-zone integrations, Physical Review. B, Solid State 13 (n.d.) 5188–5192. https://doi.org/10.1103/PhysRevB.13.5188.
[56] G. Henkelman, B.P. Uberuaga, H. Jónsson, Climbing image nudged elastic band method for finding saddle points and minimum energy paths, J Chem Phys 113 (n.d.) 9901–9904. https://doi.org/10.1063/1.1329672.
[57] R.A. Holt, Comments on the beta to alpha phase transformation in zircaloy-4, Journal of Nuclear Materials 47 (n.d.) 262–264. https://doi.org/10.1016/0022-3115(73)90111-6.
[58] C.M. Lee, Y.-K. Mok, D.-S. Sohn, High-temperature steam oxidation and oxide crack effects of Zr-1Nb-1Sn-0.1Fe fuel cladding, Journal of Nuclear Materials 496 (n.d.) 343–352. https://doi.org/10.1016/j.jnucmat.2017.10.013.
[59] H.-G. Kim, I.-H. Kim, B.-K. Choi, J.-Y. Park, A study of the breakaway oxidation behavior of zirconium cladding materials, Journal of Nuclear Materials 418 (n.d.) 186–197. https://doi.org/10.1016/j.jnucmat.2011.06.039.
[60] C.M. Lee, Y.K. Mok, D.S. Sohn, High-temperature steam oxidation and oxide crack effects of Zr-1Nb-1Sn-0.1Fe fuel cladding, Journal of Nuclear Materials 496 (2017) 343–352. https://doi.org/10.1016/j.jnucmat.2017.10.013.
[61] A.N. Wilhelm, E.A. Garcia, Simulation of oxidation phenomena during high temperature transients: Application to zirconium alloys in steam, Materials Science and Engineering 87 (1987) 73–79. https://doi.org/10.1016/0025-5416(87)90362-4.
[62] P.M. Srikumar Banerjee, Phase Transformations: Examples from Titanium and Zirconium Alloys, Elsevier Science, Oxford, 2010.
[63] H.G. Kim, I.H. Kim, B.K. Choi, J.Y. Park, A study of the breakaway oxidation behavior of zirconium cladding materials, Journal of Nuclear Materials 418 (2011) 186–197. https://doi.org/10.1016/j.jnucmat.2011.06.039.

[64] Y.H. Jeong, H.G. Kim, T.H. Kim, Effect of b phase, precipitate and Nb-concentration in matrix on corrosion and oxide characteristics of Zr-xNb alloys, Journal of Nuclear Materials 317 (n.d.) 1–12.
[65] M. Moorehead, Z. Yu, L. Borrel, J. Hu, Z. Cai, A. Couet, Comprehensive investigation of the role of Nb on the oxidation kinetics of Zr-Nb alloys, Corros Sci 155 (n.d.) 173–181. https://doi.org/10.1016/j.corsci.2019.04.017.
[66] D. Pêcheur, F. Lefebvre, A.T. Motta, C. Lemaignan, J.F. Wadier, Precipitate evolution in the Zircaloy-4 oxide layer, Journal of Nuclear Materials 189 (n.d.) 318–332. https://doi.org/10.1016/0022-3115(92)90385-X.
[67] J. Liu, High resolution structural analysis of irradiated zirconium alloys, (2019).
[68] A. Couet, A.T. Motta, B. de Gabory, Z. Cai, Microbeam X-ray Absorption Near-Edge Spectroscopy study of the oxidation of Fe and Nb in zirconium alloy oxide layers, Journal of Nuclear Materials 452 (n.d.) 614–627. https://doi.org/10.1016/j.jnucmat.2014.05.047.
[69] I. Barin, F. Sauert, E. Schultze-Rhonhof, W.S. Shen, Thermochemical data of pure substances, 2nd ed, VCH, Weinheim, 1993.
[70] S.C. Lumley, S.T. Murphy, P.A. Burr, R.W. Grimes, P.R. Chard-Tuckey, M.R. Wenman, The stability of alloying additions in Zirconium, Journal of Nuclear Materials 437 (2013) 122–129. https://doi.org/10.1016/j.jnucmat.2013.01.335.
[71] Y. Uk Kwon, J. D. Corbett, Chemistry in polar intermetallic compounds. The interstitial chemistry of zirconium-tin (Zr5Sn3), Chemistry of Materials 4 (2002) 1348–1355. https://doi.org/10.1021/cm00024a040.
[72] G. Gran, S. Andersson, The crystal structures of Zr5Sn3 and Zr3Sn, 14 (1960) 956–957.
[73] H. Okuda, S. Ochiai, The Effects of Solute and Vacancy Depletion on the Formation of Precipitation-Free Zone in a Model Binary Alloy Examined by a Monte Carlo Simulation, Mater Trans 45 (2004) 1455–1460. https://doi.org/10.2320/matertrans.45.1455.
[74] S. Kondo, Y.W. Chai, K. Kanai, L. Dosung, M. Watanabe, S. Ishikawa, T. Yamasita, Y. Kimura, Intermetallic phase precipitation and oxidation behavior of Fe–20Cr–0.5Nb–2Mo (at%) high-Cr ferritic alloy at high temperatures, Acta Mater 246 (n.d.) 118677. https://doi.org/10.1016/j.actamat.2023.118677.
[75] V.I. Baykov, R.J. Perez, P.A. Korzhavyi, B. Sundman, B. Johansson, Structural stability of intermetallic phases in the Zr-Sn system, Scr Mater 55 (2006) 485–488. https://doi.org/10.1016/j.scriptamat.2006.04.047.
[76] Y. Uk Kwon, J. D. Corbett, Chemistry in polar intermetallic compounds. The interstitial chemistry of zirconium-tin (Zr5Sn3), Chemistry of Materials 4 (2002) 1348–1355. https://doi.org/10.1021/cm00024a040.
[77] R. Jerlerud Pérez, C. Toffolon-Masclet, J.-M. Joubert, B. Sundman, The Zr–Sn binary system: New experimental results and thermodynamic assessment, Calphad 32 (n.d.) 593–601. https://doi.org/10.1016/j.calphad.2008.04.001.
[78] S. Liu, Y. Zhan, J. Wu, X. Wei, Insight into structural, mechanical, electronic and thermodynamic properties of intermetallic phases in Zr–Sn system from first-principles calculations, J Phys Chem Solids 86 (n.d.) 177–185.

https://doi.org/10.1016/j.jpcs.2015.07.009.
[79] O.T. Woo, G.J.C. Carpenter, Radiation-induced precipitation in Zircaloy-2, Journal of Nuclear Materials 159 (n.d.) 397–404. https://doi.org/10.1016/0022-3115(88)90106-7.
[80] J. Sayers, S. Lozano-Perez, S.R. Ortner, The progress of SPP oxidation in zircaloy-4 and its relation to corrosion and hydrogen pickup, (2019). https://doi.org/10.1016/j.corsci.2019.06.027.
[81] W. Qin, C. Nam, H.L. Li, J.A. Szpunar, Tetragonal phase stability in ZrO2 film formed on zirconium alloys and its effects on corrosion resistance, Acta Mater 55 (n.d.) 1695–1701. https://doi.org/10.1016/j.actamat.2006.10.030.
[82] J. Hu, J. Liu, S. Lozano-Perez, C.R.M. Grovenor, M. Christensen, W. Wolf, E. Wimmer, E. V. Mader, Hydrogen pickup during oxidation in aqueous environments: The role of nano-pores and nano-pipes in zirconium oxide films, Acta Mater 180 (2019) 105–115. https://doi.org/10.1016/j.actamat.2019.09.005.
[83] B. Cox, Some thoughts on the mechanisms of in-reactor corrosion of zirconium alloys, Journal of Nuclear Materials 336 (2005) 331–368. https://doi.org/10.1016/j.jnucmat.2004.09.029.
[84] G. David, R. Geschier, C. Roy, Etude de la croissance de l’oxyde sur le zirconium et le zircaloy-2, Journal of nuclear materials 38 (n.d.) 329–339. https://doi.org/10.1016/0022-3115(71)90062-6.
[85] A.J.G. Maroto, R. Bordoni, M. Villegas, A.M. Olmedo, M.A. Blesa, A. Iglesias, P. Koenig, Growth and characterization of oxide layers on zirconium alloys, Journal of Nuclear Materials 229 (n.d.) 79–92. https://doi.org/10.1016/0022-3115(95)00233-2.
[86] G. Jiang, D. Xu, W. Yang, L. Liu, Y. Zhi, J. Yang, High-temperature corrosion of Zr–Nb alloy for nuclear structural materials, Progress in Nuclear Energy 154 (2022). https://doi.org/10.1016/j.pnucene.2022.104490.
[87] L. Wu, V.O. Kharchenko, X. Kong, D.O. Kharchenko, DFT calculations of solute-vacancy binding in Zirconium-based Zr–Nb–Sn alloy, Nuclear Materials and Energy 32 (2022). https://doi.org/10.1016/j.nme.2022.101221.
[88] H. Okamoto, Nb-Zr (niobium-zirconium), Journal of Phase Equilibria 13 (1992) 577.
[89] H.G. Kim, B.K. Choi, J.Y. Park, Y.H. Jeong, Influence of the manufacturing processes on the corrosion of Zr-1.1Nb-0.05Cu alloy, Corros Sci 51 (2009) 2400–2405. https://doi.org/10.1016/j.corsci.2009.06.023.
[90] J.-Y. Park, B.-K. Choi, S.J. Yoo, Y.H. Jeong, Corrosion and oxide properties of HANA alloys, J ASTM Int 5 (2008) 1–13.
[91] N.A.P. Kiran Kumar, J.A. Szpunar, EBSD studies on microstructure and crystallographic orientation of δ-hydrides in Zircaloy-4, Zr–1% Nb and Zr–2.5% Nb, Mater Sci Eng A Struct Mater 528 (n.d.) 6366–6374. https://doi.org/10.1016/j.msea.2011.05.022.